Research Article Vol. 9, No. 1 | 1 Jan 2018 | BIOMEDICAL OPTICS EXPRESS 276

Biomedical Optics EXPRESS

Multispectral photoacoustic microscopy of lipids using a pulsed supercontinuum laser

TAKASHI BUMA,[1,*] NICOLE C. CONLEY,[1] AND SANG WON CHOI[1,2]

[1]*Department of Electrical, Computer, and Biomedical Engineering, Union College, Schenectady, NY 12308, USA*
[2]*Currently with the Department of Biomedical Engineering, University of Michigan, Ann Arbor, MI 48109, USA*
**bumat@union.edu*

Abstract: We demonstrate optical resolution photoacoustic microscopy (OR-PAM) of lipid-rich tissue between 1050–1714 nm using a pulsed supercontinuum laser based on a large-mode-area photonic crystal fiber. OR-PAM experiments of lipid-rich samples show the expected optical absorption peaks near 1210 and 1720 nm. These results show that pulsed supercontinuum lasers are promising for OR-PAM applications such as label-free histology of lipid-rich tissue and imaging small animal models of disease.

OCIS codes: (060.5295) Photonic crystal fibers; (110.5120) Photoacoustic imaging; (190.4370) Nonlinear optics, fibers; (320.6629) Supercontinuum generation.

References and links

1. A. Zumbusch, G. R. Holtom, and X. S. Xie, "Three-Dimensional Vibrational Imaging by Coherent Anti-Stokes Raman Scattering," Phys. Rev. Lett. **82**(20), 4142–4145 (1999).
2. C. W. Freudiger, W. Min, B. G. Saar, S. Lu, G. R. Holtom, C. He, J. C. Tsai, J. X. Kang, and X. S. Xie, "Label-free biomedical imaging with high sensitivity by stimulated Raman scattering microscopy," Science **322**(5909), 1857–1861 (2008).
3. T. B. Huff and J.-X. Cheng, "In vivo coherent anti-Stokes Raman scattering imaging of sciatic nerve tissue," J. Microsc. **225**(2), 175–182 (2007).
4. C.-R. Hu, D. Zhang, M. N. Slipchenko, J.-X. Cheng, and B. Hu, "Label-free real-time imaging of myelination in the Xenopus laevis tadpole by in vivo stimulated Raman scattering microscopy," J. Biomed. Opt. **19**(8), 086005 (2014).
5. M. J. den Broeder, M. J. B. Moester, J. H. Kamstra, P. H. Cenijn, V. Davidoiu, L. M. Kamminga, F. Ariese, J. F. de Boer, and J. Legler, "Altered adipogenesis in zebrafish larvae following high fat diet and chemical exposure is visualized by stimulated Raman scattering microscopy," Int. J. Mol. Sci. **18**(4), 894 (2017).
6. C.-H. Chien, W.-W. Chen, J.-T. Wu, and T.-C. Chang, "Label-free imaging of Drosophila in vivo by coherent anti-Stokes Raman scattering and two-photon excitation autofluorescence microscopy," J. Biomed. Opt. **16**(1), 016012 (2011).
7. H. F. Zhang, K. Maslov, G. Stoica, and L. V. Wang, "Functional photoacoustic microscopy for high-resolution and noninvasive in vivo imaging," Nat. Biotechnol. **24**(7), 848–851 (2006).
8. J. Yao and L. V. Wang, "Sensitivity of photoacoustic microscopy," Photoacoustics **2**(2), 87–101 (2014).
9. K. Maslov, H. F. Zhang, S. Hu, and L. V. Wang, "Optical-resolution photoacoustic microscopy for in vivo imaging of single capillaries," Opt. Lett. **33**(9), 929–931 (2008).
10. S. Ye, R. Yang, J. Xiong, K. K. Shung, Q. Zhou, C. Li, and Q. Ren, "Label-free imaging of zebrafish larvae in vivo by photoacoustic microscopy," Biomed. Opt. Express **3**(2), 360–365 (2012).
11. K. Jansen, M. Wu, A. F. W. van der Steen, and G. van Soest, "Photoacoustic imaging of human coronary atherosclerosis in two spectral bands," Photoacoustics **2**(1), 12–20 (2014).
12. B. Wang, A. Karpiouk, D. Yeager, J. Amirian, S. Litovsky, R. Smalling, and S. Emelianov, "Intravascular photoacoustic imaging of lipid in atherosclerotic plaques in the presence of luminal blood," Opt. Lett. **37**(7), 1244–1246 (2012).
13. T. J. Allen, A. Hall, A. P. Dhillon, J. S. Owen, and P. C. Beard, "Spectroscopic photoacoustic imaging of lipid-rich plaques in the human aorta in the 740 to 1400 nm wavelength range," J. Biomed. Opt. **17**(6), 061209 (2012).
14. H.-W. Wang, N. Chai, P. Wang, S. Hu, W. Dou, D. Umulis, L. V. Wang, M. Sturek, R. Lucht, and J.-X. Cheng, "Label-free bond-selective imaging by listening to vibrationally excited molecules," Phys. Rev. Lett. **106**(23), 238106 (2011).
15. X. Bai, X. Gong, W. Hau, R. Lin, J. Zheng, C. Liu, C. Zeng, X. Zou, H. Zheng, and L. Song, "Intravascular optical-resolution photoacoustic tomography with a 1.1 mm diameter catheter," PLoS One **9**(3), e92463 (2014).
16. T. P. Matthews, C. Zhang, D.-K. Yao, K. Maslov, and L. V. Wang, "Label-free photoacoustic microscopy of peripheral nerves," J. Biomed. Opt. **19**(1), 016004 (2014).

#310041 https://doi.org/10.1364/BOE.9.000276
Journal © 2018 Received 25 Oct 2017; revised 30 Nov 2017; accepted 16 Dec 2017; published 19 Dec 2017

17. P. Wang, J. R. Rajian, and J.-X. Cheng, “Spectroscopic imaging of deep tissue through photoacoustic detection of molecular vibration,” J. Phys. Chem. Lett. **4**(13), 2177–2185 (2013).
18. T. Buma, B. C. Wilkinson, and T. C. Sheehan, “Near-infrared spectroscopic photoacoustic microscopy using a multi-color fiber laser source,” Biomed. Opt. Express **6**(8), 2819–2829 (2015).
19. T. Buma, J. L. Farland, and M. R. Ferrari, “Near-infrared multispectral photoacoustic microscopy using a graded-index fiber amplifier,” Photoacoustics **4**(3), 83–90 (2016).
20. P. Hajireza, A. Forbrich, and R. Zemp, “In-vivo functional optical-resolution photoacoustic microscopy with stimulated Raman scattering fiber-laser source,” Biomed. Opt. Express **5**(2), 539–546 (2014).
21. E. M. Strohm, M. J. Moore, and M. C. Kolios, “High resolution ultrasound and photoacoustic imaging of single cells,” Photoacoustics **4**(1), 36–42 (2016).
22. W. Wadsworth, N. Joly, J. Knight, T. Birks, F. Biancalana, and P. Russell, “Supercontinuum and four-wave mixing with Q-switched pulses in endlessly single-mode photonic crystal fibres,” Opt. Express **12**(2), 299–309 (2004).
23. G. Agrawal, *Nonlinear Fiber Optics, 4th ed*., Academic Press, 2006.
24. J. M. Dudley, G. Genty, and S. Coen, “Supercontinuum generation in photonic crystal fiber,” Rev. Mod. Phys. **78**(4), 1135–1184 (2006).
25. S. Coen, A. H. L. Chau, R. Leonhardt, J. D. Harvey, J. C. Knight, W. J. Wadsworth, and P. S. J. Russell, “White-light supercontinuum generation with 60-ps pump pulses in a photonic crystal fiber,” Opt. Lett. **26**(17), 1356–1358 (2001).
26. Y. N. Billeh, M. Liu, and T. Buma, “Spectroscopic photoacoustic microscopy using a photonic crystal fiber supercontinuum source,” Opt. Express **18**(18), 18519–18524 (2010).
27. C. Lee, M. Jeon, M. Y. Jeon, J. Kim, and C. Kim, “In vitro photoacoustic measurement of hemoglobin oxygen saturation using a single pulsed broadband supercontinuum laser source,” Appl. Opt. **53**(18), 3884–3889 (2014).
28. X. Shu, M. Bondu, B. Dong, A. Podoleanu, L. Leick, and H. F. Zhang, “Single all-fiber-based nanosecond-pulsed supercontinuum source for multispectral photoacoustic microscopy and optical coherence tomography,” Opt. Lett. **41**(12), 2743–2746 (2016).
29. M. Bondu, C. Brooks, C. Jakobsen, K. Oakes, P. M. Moselund, L. Leick, O. Bang, and A. Podoleanu, “High energy supercontinuum sources using tapered photonic crystal fibers for multispectral photoacoustic microscopy,” J. Biomed. Opt. **21**(6), 061005 (2016).
30. G. M. Hale and M. R. Querry, “Optical constants of water in the 200-nm to 200-μm wavelength region,” Appl. Opt. **12**(3), 555–563 (1973).
31. R. R. Anderson, W. Farinelli, H. Laubach, D. Manstein, A. N. Yaroslavsky, J. Gubeli 3rd, K. Jordan, G. R. Neil, M. Shinn, W. Chandler, G. P. Williams, S. V. Benson, D. R. Douglas, and H. F. Dylla, “Selective photothermolysis of lipid-rich tissues: a free electron laser study,” Lasers Surg. Med. **38**(10), 913–919 (2006).
32. Datasheet for LMA-PM-10, NKT Photonics, Inc.
33. J. Hui, R. Li, E. H. Phillips, C. J. Goergen, M. Sturek, and J.-X. Cheng, “Bond-selective photoacoustic imaging by converting molecular vibration into acoustic waves,” Photoacoustics **4**(1), 11–21 (2016).
34. E. L. Arrese and J. L. Soulages, “Insect fat body: energy, metabolism, and regulation,” Annu. Rev. Entomol. **55**(1), 207–225 (2010).
35. J. C. Travers, “Blue extension of optical fibre supercontinuum generation,” J. Opt. **12**(11), 113001 (2010).
36. G. Genty, T. Ritari, and H. Ludvigsen, “Supercontinuum generation in large mode-area microstructured fibers,” Opt. Express **13**(21), 8625–8633 (2005).
37. Q. Chen, T. Jin, W. Qi, X. Mo, and L. Xi, “Label-free photoacoustic imaging of the cardio-cerebrovascular development in the embryonic zebrafish,” Biomed. Opt. Express **8**(4), 2359–2367 (2017).

---

1. Introduction

High resolution label-free imaging of lipids has many applications in medicine and developmental biology. Optical techniques typically produce label-free contrast by probing the vibrational modes of lipid molecules. Spectroscopic imaging of lipids with sub-micron spatial resolution has been demonstrated with nonlinear optical techniques such as coherent anti-Stokes Raman scattering (CARS) [1] and stimulated Raman scattering (SRS) microscopy [2]. These methods have demonstrated label-free imaging of murine sciatic nerve tissue [3], myelination in Xenopus tadpoles [4], adipogenesis in zebrafish larvae [5], and fat bodies in Drosophila larvae [6]. However, the limited penetration depth (≈100 μm) of CARS and SRS microscopy can be an issue for in vivo imaging and thick tissue samples.

Photoacoustic microscopy (PAM) is a hybrid technique using pulsed laser excitation and ultrasonic detection [7, 8]. Label-free image contrast is based on linear optical absorption in tissue. Optical resolution PAM (OR-PAM) achieves μm-scale lateral resolution by focusing the laser excitation, while fine axial resolution (< 75 μm) is produced by using nanosecond laser pulses and high frequency detection transducers (e.g. >20 MHz) [9]. OR-PAM has superior penetration depth (≈1 mm) but inferior spatial resolution compared to CARS and

SRS microscopy. Nevertheless, the spatial resolution of OR-PAM is sufficient to perform label-free imaging of individual capillaries in mice [9] and microvasculature in zebrafish larvae [10].

Label-free PAM of lipid-rich tissue, such as atherosclerotic plaques [11–15] and myelinated peripheral nerves [16, 17], require near-infrared laser pulses near 1720 or 1210 nm. These wavelengths are the first and second overtone optical absorption resonances of C-H bonds in lipids [17]. Laser pulses at these two wavelengths typically require expensive optical parametric oscillators (OPOs). OPOs produce mJ pulse energies over a very wide wavelength range. However, their high cost is a major drawback for OR-PAM applications that typically require pulse energies on the μJ scale.

We have been developing more cost-effective lasers based on nonlinear fiber optics. OR-PAM of lipids at wavelengths between 1050 – 1350 nm can be performed with standard solid-state Nd pulsed lasers and cascaded SRS in a silica fiber [18, 19]. Similar approaches have also been demonstrated with visible lasers for OR-PAM involving blood oxygenation and single cell studies [20, 21]. A disadvantage of cascaded SRS is the difficulty in generating 1700 nm light in silica optical fiber. SRS is typically the dominant nonlinear effect when nanosecond laser pulses propagate in the presence of positive (normal) dispersion [22]. However, most optical fibers have negative (anomalous) dispersion at wavelengths longer than 1300 nm [23]. Therefore, SRS in silica optical fiber is not an effective approach to generating nanosecond pulses near 1700 nm for OR-PAM of lipids.

A more promising approach is supercontinuum generation. Unlike the discrete spectral peaks produced by SRS, the broad and smooth spectrum produced by supercontinuum generation can extend from visible wavelengths (e.g. 500 nm) to beyond 1800 nm. Negative dispersion is an essential condition for supercontinuum generation, which is a highly complex process involving several nonlinear effects such as modulation instability, soliton generation and self-frequency shift, and dispersive wave generation [24]. One of the most efficient methods of supercontinuum generation is to use photonic crystal fibers (PCFs), which have a honeycomb-like microstructure to produce a desired chromatic dispersion [25]. Previous work in PCF-based supercontinuum sources for OR-PAM have concentrated on visible wavelengths (e.g. < 800 nm) [26–29]. We demonstrate in this paper, for the first time to our knowledge, OR-PAM of lipids using the longer wavelengths (e.g. > 1200 nm) produced by a supercontinuum laser using commercially available PCF.

2. Methods

2.1 Pulsed supercontinuum laser

A schematic of our pulsed supercontinuum laser is shown in Fig. 1(a). The pump laser is an actively Q-switched 1047 nm Nd:YLF laser (CrystaLaser) producing 100 μJ pulses with a 14 ns pulse duration and 2.5 kHz repetition rate. An aspherical lens couples the pump light into a 30 meter long polarization-maintaining large mode-area PCF (LMA-PM-10, NKT Photonics). A half-wave plate (HWP) adjusts the orientation of the pump laser polarization to be parallel to the fast axis of the fiber. The fiber coupling efficiency is approximately 30%. The fiber output is collimated with a 10X microscope objective.

2.2 OR-PAM system

Our transmission-mode OR-PAM system selects the desired laser wavelength with a filter wheel containing six dielectric bandpass filters at 1050, 1100, 1225, 1325, 1600, and 1714 nm. These wavelengths were chosen to vary the contrast between lipids and water using readily available off-the-shelf bandpass filters. Images at 1225 and 1714 nm should highlight fat, since lipids have stronger optical absorption than water at these wavelengths (Fig. 1(b)). Images at 1325 and 1600 nm should highlight non-fatty tissue due to the stronger optical absorption of water than lipids at these wavelengths. Little image contrast is expected at 1050 and 1100 nm, where both lipids and water have low optical absorption. The 1050 nm filter has a 10 nm bandwidth and 80% transmission. All other filters have a 50 nm bandwidth and 80% transmission. The low spectral energy density of the pulsed supercontinuum requires wider bandwidth filters to produce µJ pulse energies at most wavelengths. The selected wavelength is focused with a 4X microscope objective (Olympus). The photoacoustic signal is detected by a 25 MHz f/2 transducer (Olympus NDT). The transducer signal goes through a 60 dB (Miteq) amplifier and 50 MHz low pass filter (Mini-Circuits) before acquisition with a 250 MS/sec 8-bit digitizer board (National Instruments). A computer-controlled motorized positioner (Velmex) performs two-dimensional scanning of the sample. Data acquisition is performed with LabVIEW (National Instruments) while data processing and reconstruction are performed off-line in MATLAB (Mathworks).

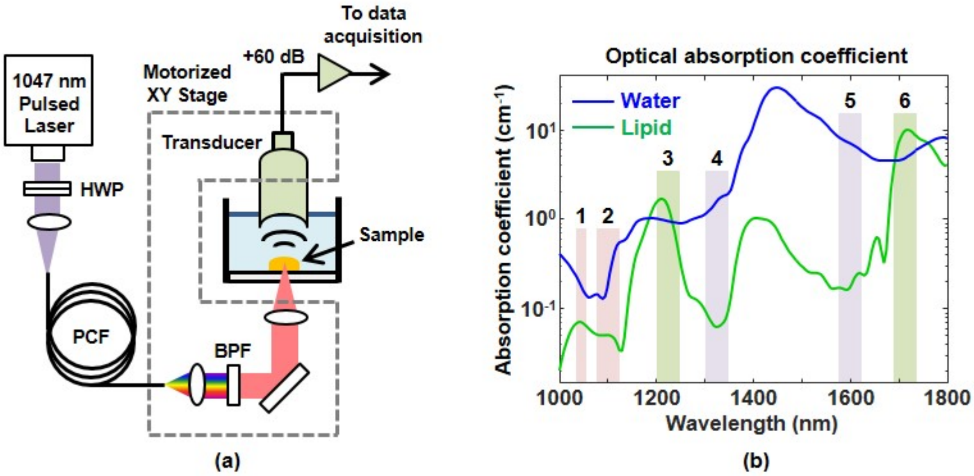

Fig. 1. (a) Schematic of pulsed supercontinuum laser and OR-PAM setup. The half-wave plate (HWP) adjusts the pump laser polarization to be parallel with the fast axis of the photonic crystal fiber (PCF). The desired wavelength band for OR-PAM is selected with a dielectric bandpass filter (BPF). (b) Optical absorption coefficient of water (blue) and lipid (green) from 1000 – 1800 nm [30, 31]. Rectangular bars show the passbands of the six bandpass filters at 1050 nm (1), 1100 nm (2), 1225 nm (3), 1325 nm (4), 1600 nm (5), and 1714 nm (6).

3. Experiments and results

3.1 Optical characterization of the fiber output

The fiber output spectrum between 1000 – 1800 nm was measured with a scanning monochromator (SDMC1-05G, Optometrics) and an InGaAs photodetector (DET05D, Thorlabs). The spectrum at full input laser power is shown in Fig. 2. The strong peak at 1047 nm is the pump (P), while the two peaks at 1098 and 1153 nm are the first (S1) and second (S2) Stokes lines due to cascaded SRS. A smooth continuum spans from 1200 – 1800 nm. All these features are consistent with the 1200 nm zero-dispersion wavelength of the PCF [32]. Cascaded SRS dominates for wavelengths shorter than 1200 nm (positive fiber dispersion) while supercontinuum generation dominates for wavelengths longer than 1200 nm (negative fiber dispersion). The dip near 1200 nm is indicative of SRS suppression due to competition from phase matched four wave mixing (FWM) [23].

3.2 OR-PAM characterization

The supercontinuum is sent through a dielectric bandpass filter at 1050, 1100, 1225, 1325, 1600 or 1714 nm. A thermal sensor (S401C, Thorlabs) was used to measure the average pulse energy after each bandpass filter. As shown in Table 1, the pulse energy is above 1 µJ at all wavelength bands except 1600 and 1714 nm. Although the low pulse energy at 1714 nm is most likely insufficient for practical applications, proof-of-concept OR-PAM of lipids is still possible.

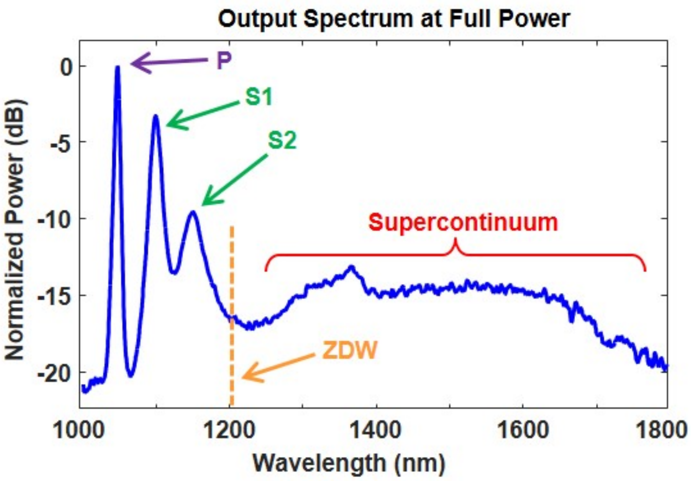

Fig. 2. Fiber output spectrum at full input power. The three distinct peaks are the pump (P), first Stokes (S1), and second Stokes (S2) lines. The dashed vertical line at 1200 nm marks the PCF zero-dispersion wavelength (ZDW). The broad continuum extends from 1200 to 1800 nm.

Table 1. Pulse Energy and Spatial Resolution vs Band-Pass Filter

Filter Center Wavelength (nm)	1050	1100	1225	1325	1600	1714
Filter Bandwidth (nm)	10	50	50	50	50	50
Pulse Energy (μJ)	6.81	6.43	1.07	1.23	0.76	0.32
Measured resolution (water) (μm)	14.5	15.2	15.4	15.2	15.7	15.9
Theoretical resolution (μm)	14.0	14.0	14.1	14.3	14.6	14.8
Resolution in diluted milk (μm)	18.7	16.2	17.5	18.5	17.1	17.0
Depth resolution (μm)	77	79	77	77	71	65

The lateral resolution of the OR-PAM system was characterized by imaging the edge of a bar pattern in a 1951 USAF resolution target. Measurements were performed through 1.1 mm of clear (water) and scattering (25% diluted whole milk) media. An edge spread function (ESF) was produced by curve-fitting the raw data with a smoothing spline in MATLAB. The derivative of this ESF yields the line spread function (LSF). Lateral resolution is defined as the full width at half-maximum (FWHM) of the LSF. The theoretical resolution is estimated by modeling the laser focal spot as a magnified image of the optical fiber tip according to:

$$\Delta = 2.65 MFD\sqrt{0.5\ln 2} \tag{1}$$

The mode field diameter (MFD) is the 1/e^2 width of the optical intensity distribution within the fiber. The fiber collimating 10X objective (F = 17 mm) and PAM focusing 4X objective (F = 45 mm) form a projection system with a magnification factor equal to 45/17 = 2.65. The factor of $\sqrt{0.5\ln 2}$ is necessary to scale the MFD, which is a 1/e^2 width, into a FWHM quantity. Using MFD values from the fiber data sheet [32], Table 1 shows that the measured results in water are in reasonable agreement with theory. Resolution is worse in diluted milk, where optical scattering broadens the laser focus. The data fluctuations are most likely due to reduced signal-to-noise ratio of the measurements in diluted milk.

Depth resolution was computed from the FWHM of the signal envelope from the USAF target [18]. As shown in Table 1, the depth resolution is roughly constant for 1050 – 1325 nm but improves slightly at 1600 nm and 1714 nm. This is consistent with our observation that the 1714 nm laser pulse duration is about 9 ns, which is considerably shorter than the 14 ns pump pulse. This pulse shortening is most likely a result of the highly nonlinear nature of supercontinuum generation, where the most intense portion of the pump produces the largest spread in wavelengths.

3.3 OR-PAM of lipid phantom

Multispectral OR-PAM was performed on a lipid phantom consisting of a butter droplet embedded in clear gelatin. Figure 3(a) shows en face images formed by integrating C-mode image planes over the entire butter droplet thickness. All images were signal averaged 64 times and displayed over a 20 dB scale. Images are not corrected for differences or variations in laser pulse energy. Lipid contrast is clearly highest at 1714 nm, despite these laser pulses having the lowest energy (0.32 μJ). Image contrast is slightly higher at 1225 nm compared to 1100 and 1325 nm. These results are consistent with the lipid optical absorption peaks at 1720 and 1210 nm. Optical absorption in water is higher than lipids at 1325 and 1600 nm. Therefore, image contrast at 1325 and 1600 nm is primarily due to photoacoustic generation from gelatin at the lipid-gelatin interface. Poor image contrast at 1050 nm is due to low optical absorption in both lipids and gelatin, despite laser pulses having the highest energy (6.81 μJ) at this wavelength.

B-mode image slices through the central row of the lipid phantom are shown in Fig. 3(b). All images are shown over the same 20 dB scale. The top and bottom surfaces of the butter droplet are brightest at 1714 nm and weakest at 1050 nm. Overall, the image contrast in the B-mode images are consistent with the integrated C-mode images. As a more quantitative measure of image quality, we computed the signal-to-noise ratio (SNR) of a 25 x 60 μm region within the bottom and top lipid surfaces of each B-mode image. As shown in Fig. 3(c), the SNR is highest at 1714 nm, despite the lowest pulse energy at this wavelength. A photoacoustic spectrum was obtained by analyzing the same 25 x 60 μm regions in the bottom and top lipid surfaces. The B-mode pixel amplitudes were summed together and then divided by the appropriate laser pulse energy from Table 1 to remove wavelength variations in optical fluence. Finally, the spectrum is normalized with respect to the 1714 nm component. As shown in Fig. 3(d), the spectral amplitude is highest at 1714 nm while a local maximum exists at 1225 nm.

For validation purposes, the measured photoacoustic spectrum is compared to a theoretical spectrum based on the following simplified model. Our lipid phantom consists of two optically absorbing materials (butter inside gelatin). The received signal from the bottom and top lipid surface is due to the difference in photoacoustic generation between lipid and gelatin. Therefore, the photoacoustic signal magnitude from the lipid-gelatin interface is given by:

$$S(\lambda) = \left|\beta F(\lambda)\left(\mu_{Lipid}(\lambda)\Gamma_{Lipid} - \mu_{Water}(\lambda)\Gamma_{Water}\right)\right| \tag{2}$$

where λ is the laser wavelength, β is an imaging system constant, $F(\lambda)$ is the optical fluence, $\mu(\lambda)$ is the optical absorption coefficient, and Γ is the Gruneisen parameter. We substituted butter and aqueous gelatin with lipid and water, respectively, since the material properties of lipid and water are readily available [30, 31, 33]. Both Γ_{Lipid} and Γ_{Water} are approximated as constant values in Eq. (2). The supercontinuum laser uses an optical bandpass filter, therefore Eq. (2) must be modified to include an integration within the filter passband:

$$S(\lambda_m) \approx \beta F(\lambda_m) \left| \int_{\lambda_m-\Delta\lambda/2}^{\lambda_m+\Delta\lambda/2} \left(\mu_{Lipid}(\lambda)\Gamma_{Lipid} - \mu_{Water}(\lambda)\Gamma_{Water}\right) d\lambda \right| = \beta F(\lambda_m) K(\lambda_m) \quad (3)$$

where λ_m and $\Delta\lambda$ are the center wavelength and bandwidth of the optical bandpass filter, respectively. Equation (3) approximates the optical fluence as a constant within the filter passband, allowing $F(\lambda_m)$ to be taken outside the integral. The integration term is lumped into the quantity $K(\lambda_m)$ to simplify notation. Finally, Eq. (3) is normalized with respect to the value at 1714 nm to produce $A(\lambda_m)$:

$$A(\lambda_m) = \frac{F(\lambda_m)}{F(1714)} \frac{K(\lambda_m)}{K(1714)} \approx \frac{E(\lambda_m)}{E(1714)} \frac{K(\lambda_m)}{K(1714)} \quad (4)$$

where $E(\lambda_m)$ is the laser pulse energy after the optical bandpass filter with center wavelength λ_m. In Eq. (4), the ratio of optical fluence at two wavelengths is approximated as the ratio of pulse energy, which is a better known experimental parameter. Figure 3(d) shows reasonable agreement between our simple theoretical model $A(\lambda_m)$ and the measured photoacoustic spectrum. It is worth noting that significant disagreement at 1600 nm occurs if the

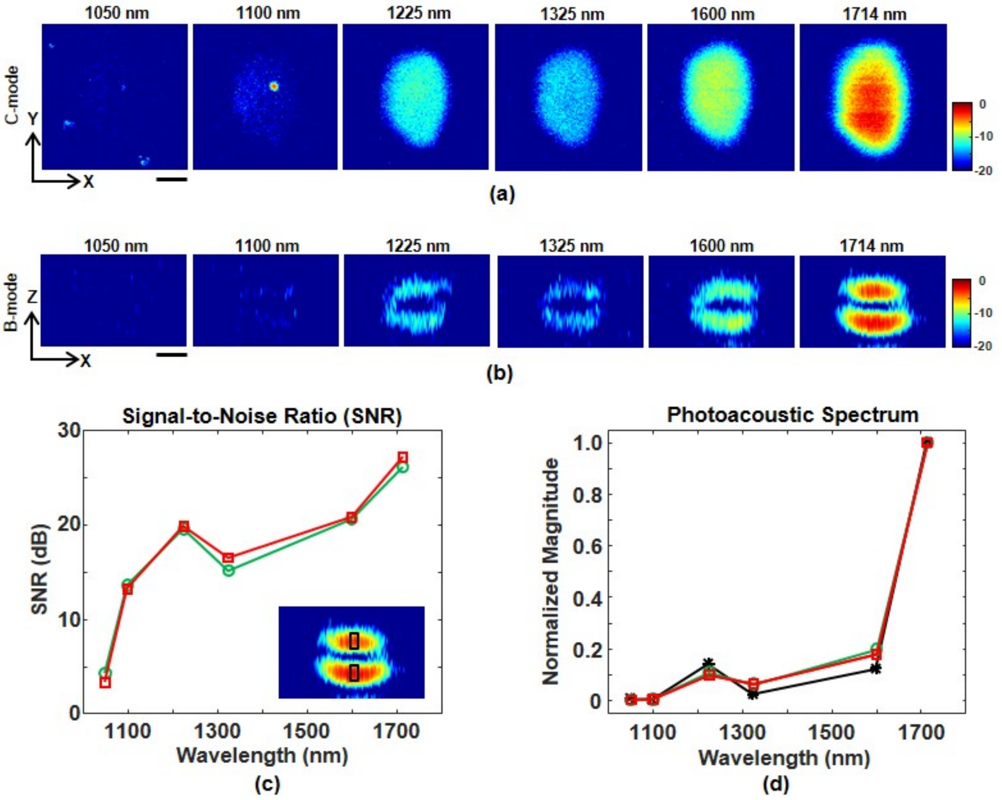

Fig. 3. (a) Multispectral en face PAM images of a lipid phantom consisting of butter inside clear gelatin. All images integrate C-mode planes over the entire butter thickness and are shown over the same 20 dB scale. (b) Multispectral B-mode slices along the central row of each image in Fig. 3(a). All slices are shown over the same 20 dB scale. The scale bars in both (a) and (b) represent 100 µm. (c) Signal-to-noise ratio (SNR) of a 25 x 60 µm region (see inset) within the bottom (red squares) and top (green circles) lipid layer in each B-mode image. (d) Measured (red squares and green circles) and theoretical (black asterisks) photoacoustic spectra of the same regions in the lipid phantom.

contribution of water is removed from our theoretical model. A more rigorous model would require detailed knowledge of gelatin and butter properties, local optical fluence, and compensation of fluctuations in laser pulse energy.

3.4 OR-PAM of intramuscular fat

Multispectral OR-PAM was also performed on a thin slice of steak embedded in clear gelatin. The beef and gelatin are each approximately 0.5 mm thick. Figure 4(a) shows en face images (XY plane) formed by integrating C-mode image planes over the entire meat thickness. All

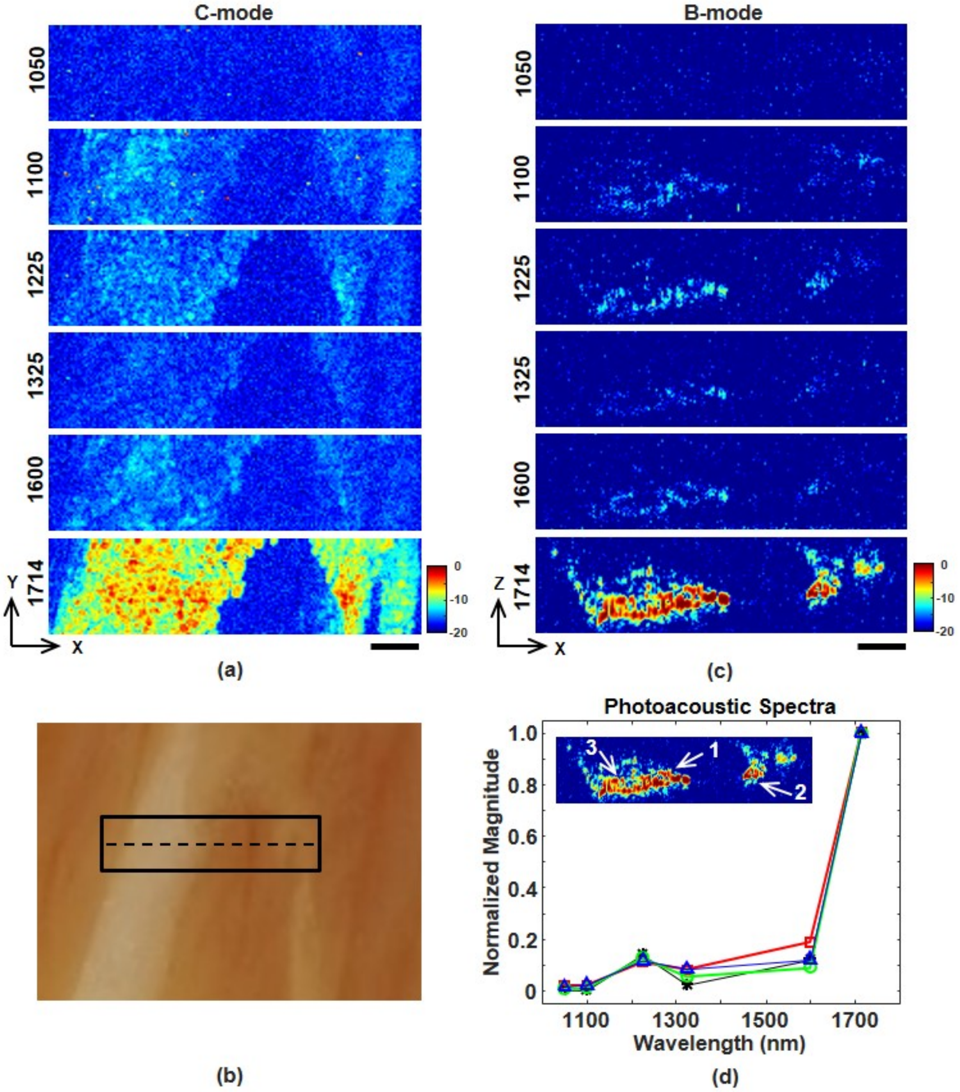

Fig. 4. (a) Multispectral en face PAM images of a thin slice of beef embedded in clear gelatin. The scale bar represents 500 µm. (b) Photograph of the beef sample. The solid rectangle outlines the C-mode region imaged by OR-PAM. (c) B-mode image slices along the dashed black line in Fig. 4(b). The scale bar represents 500 µm. (d) Photoacoustic spectra measured at three locations (see inset) within the fatty portion of the beef sample. Locations 1, 2, and 3 correspond to red squares, green circles, and blue triangles, respectively. Black asterisks are the spectrum from the simple theoretical model.

images were signal-averaged 64 times, displayed over a 20 dB scale, and are not corrected for differences or variations in laser pulse energy. As expected, the 1714 nm image shows the brightest features. Figure 4(b) shows a photo of the imaged region, where the fatty areas correlate well with the 1714 nm image in Fig. 4(a). Figure 4(c) shows B-mode slices (XZ plane) of the central row in the imaged region. All images are shown over the same 20 dB scale. Again, image contrast is clearly highest at 1714 nm. The 1225 nm image has slightly higher contrast than the 1100 and 1325 nm images.

Figure 4(d) shows photoacoustic spectra of three 25 x 60 μm regions within the fat. As expected, all three regions produce similar spectra as the butter spectrum in Fig. 3(d). There is reasonable agreement between the experimental spectra and our simplified theoretical model based on Eq. (4). Consistent with our lipid phantom results, good agreement between experiment and theory requires including photoacoustic generation from both lipid and water in our model. Accurate multispectral identification of lipids would require a more rigorous model including material properties of fat, muscle, and connective tissue as well as optical scattering and attenuation.

3.5 OR-PAM of Drosophila larva

As an example application in developmental biology, we performed multispectral OR-PAM of the fat bodies in a fixed Drosophila melanogaster larva embedded in clear gelatin. The

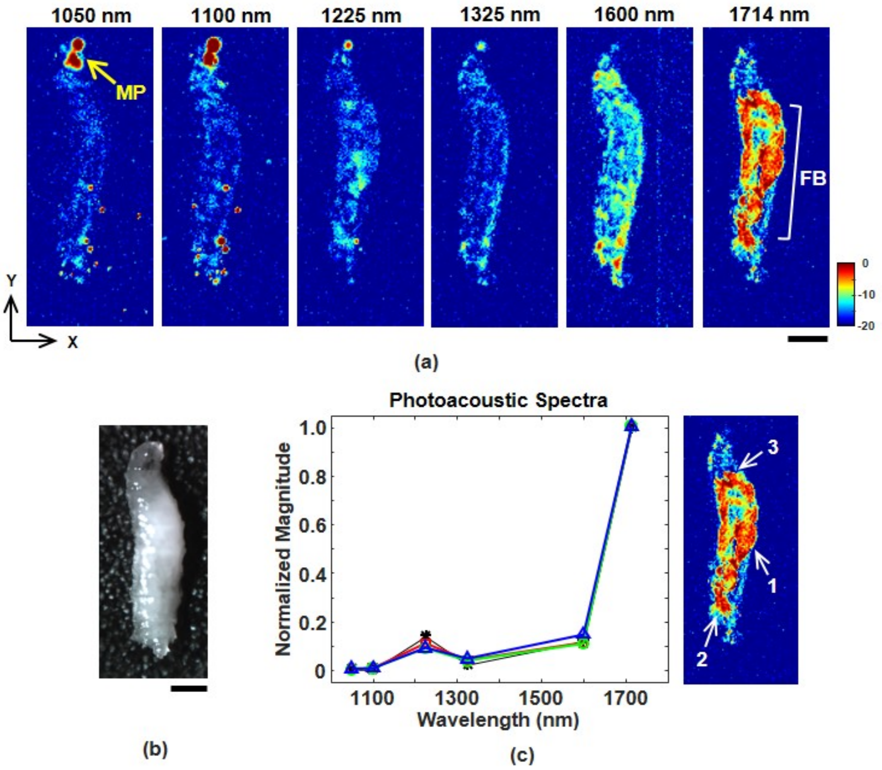

Fig. 5. (a) Multispectral OR-PAM C-mode images of a fixed third instar Drosophila larva. All images are a 60 μm thick slice and are shown over the same 20 dB scale. The scale bar represents 500 μm. The fat bodies (FB) are clearly visualized at 1714 nm. The mouth parts (MP) saturate the dynamic range of the 1050 and 1100 nm images. (b) Photograph of the larva. The scale bar represents 500 μm. (c) Photoacoustic spectra measured at three locations in the larva. Locations 1, 2, and 3 correspond to red squares, green circles, and blue triangles, respectively. Black asterisks are the spectrum from the simple theoretical model.

larval fat bodies serve a variety of functions such as energy storage and metabolism [34]. Figure 5(a) shows 60 µm thick C-mode slices through the center of the larva. Each image is signal averaged 64 times, covers a 4 x 1.6 mm field of view, and displayed over the same 20 dB scale. The image at 1714 nm clearly shows a variety of internal features, while different structures are emphasized at 1600 nm. Lipids should be well visualized at 1225 nm, but the contrast is significantly lower than at 1714 nm. Figure 5(c) shows that photoacoustic spectra at three locations inside the larva are consistent with our theoretical model based on Eq. (4). The saturated regions at the top of the 1050 and 1100 nm images are due to melanin in the mouth parts. These same regions are much fainter at longer wavelengths. This suggests that imaging at short and long wavelengths (e.g. 1050 and 1714 nm) can produce a strong reversal in image contrast between lipids and melanin.

4. Discussion

In order to gain a better understanding of our pulsed supercontinuum laser, we monitored the fiber output spectrum from 600 – 1800 nm while varying the input laser pulse energy. The spectrum from 1000 – 1800 nm was measured with the same instrumentation described previously, while the spectrum from 600 – 1000 nm was measured with a CCD spectrometer (CCS175, Thorlabs). Figure 6 shows both sets of spectra, where the logarithmic scale of each set is adjusted to more easily visualize important features. When the input pulse energy steadily increases from 0 to 30 µJ, Stokes lines S1 and S2 appear in a sequential manner consistent with cascaded SRS. Increasing the input pulse energy past 40 µJ produces a Stokes line S3′ near 1360 nm and an anti-Stokes peak AS3′ near 850 nm. The sidebands broaden into a continuum at higher input pulse energies.

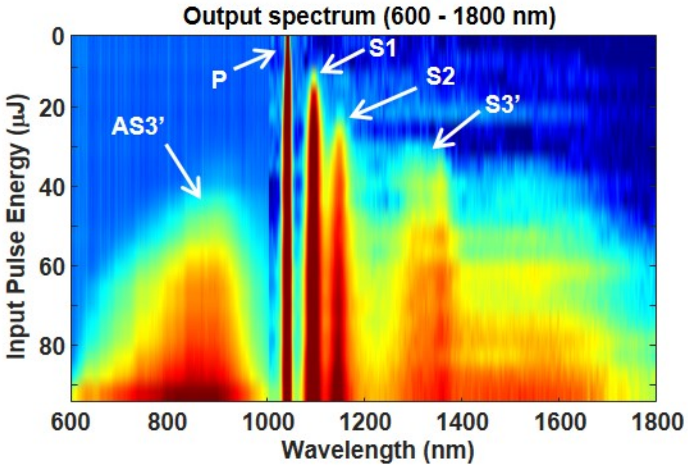

Fig. 6. Fiber output spectrum as a function of input laser energy. The pump (P) is clearly visible at 1047 nm, as well as two Stokes lines S1 (1098 nm) and S2 (1153 nm). The wide peak near 1350 nm (S3′) evolves into a broad continuum from 1200 – 1800 nm. The broad peak near 900 nm (AS3′) evolves into a continuum from 600 – 1000 nm.

Figure 6 suggests that sidebands S3′ and AS3′ are due to phase-matched FWM [22, 24]. The initial broadening of S3′ is probably due to soliton generation from modulation instability. These solitons undergo a variety of frequency shifting and broadening processes [24]. Meanwhile, AS3′ seeds the production of dispersive waves that can couple with the solitons produced by S3′, leading to additional spectral broadening of both sidebands [35]. Our observations differ from Genty [36], where supercontinuum generation in a large mode-area PCF was seeded by the third Stokes line from cascaded SRS. This discrepancy may be due to our shorter pump laser wavelength as well as the high birefringence of our polarization-maintaining PCF. The importance of pump polarization effects were confirmed by our observation that the broadest supercontinuum requires the pump laser to be aligned with the fast axis of the fiber.

Supercontinuum generation is generally most efficient when the pump laser wavelength is slightly longer than the zero-dispersion wavelength of the fiber [24]. However, our pump laser (1047 nm) is much shorter than our fiber's zero-dispersion wavelength (1200 nm). Although this wavelength mismatch is not optimal, a large mode-area PCF is scalable to higher pulse energies [36]. The wavelength versatility of our current pulsed supercontinuum laser is a major advantage for multispectral OR-PAM. Practical applications require µJ-level pulse energies at any given wavelength [14, 15]. The low spectral energy density (6.4 nJ/nm) at 1714 nm is an important limitation of our current system. A narrower bandwidth filter (e.g. 10 nm) should improve spectral identification of lipids. Therefore, we must increase our laser's spectral energy density at 1714 nm by roughly 20-fold for practical applications.

This can be achieved with a multi-pronged approach combining a higher energy pump laser, improved fiber coupling efficiency, and a longer PCF. Figure 6 suggests that further increasing the input pulse energy should produce more output energy at 1714 nm. We have not observed optical damage to the fiber tip when doubling the numerical aperture of the coupling lens. This suggests that increasing the pump pulse energy by 4-fold should not damage the fiber. Furthermore, our 30% fiber coupling efficiency is about a factor of two lower than other studies using large-mode area PCF [29]. An insufficiently long fiber results in a narrower supercontinuum, although the spectral extent eventually saturates with fiber length [24]. Theoretically, PCF-based supercontinuum sources can produce spectra that extend to 2000 nm [35]. Figure 2 and Fig. 6 show that the red-wavelength edge of our supercontinuum is near 1800 nm. Therefore, a longer fiber (e.g. 100 m) should extend the red-wavelength edge of the supercontinuum and result in a roughly 3-fold increase in spectral energy density at 1714 nm. Therefore, the combination of a higher energy pump laser, improved coupling efficiency, and a longer fiber should produce a 20-fold increase in spectral energy density at 1714 nm.

The optical fluence at the laser focus is estimated to be 280 mJ/cm^2 at 1714 nm for our current OR-PAM system. Increasing the 1714 nm pulse energy to the µJ level will result in a fluence of roughly 1 J/cm^2 at the laser focus. This is not unusual for OR-PAM, although it is considerably higher than safety limitations on surface optical fluence [9, 14]. Such high fluences may not be a major issue for ex vivo applications such as label-free pathology, but it could pose a concern for in vivo applications. It is worth noting that the optical absorption coefficient of lipids at 1714 nm is roughly 100-fold lower than hemoglobin and melanin at visible wavelengths. This reduces the likelihood of photothermal tissue damage [8].

Our system currently has lateral and axial spatial resolution of 15 µm and 75 µm, respectively. Although sufficient to visualize the larger organs inside a Drosophila larva, spatial resolution should be improved by at least 3-fold for practical applications in developmental biology [10, 14, 37]. Lateral resolution can be improved to 5 µm by expanding the diameter of the collimated laser beam and switching to a 10X microscope objective. Axial resolution can be improved by upgrading to a higher frequency detection transducer (e.g. 75 MHz).

Another practical issue for OR-PAM is pulse-to-pulse stability, which is particularly important for imaging without signal averaging. We quantified pulse stability by measuring the energy of 10,000 laser pulses at each filter wavelength. For each wavelength, a histogram was constructed from the pulse energies normalized with respect to their mean value. The resulting histograms in Fig. 7 clearly show significant variation at all wavelengths. The standard deviation for each measurement set is 0.22, 0.27, 0.61, 0.40, 0.48, and 0.49 at 1050, 1100, 1225, 1325, 1600, and 1714 nm, respectively. Somewhat surprising is that the broadest distribution occurs at 1225 nm. This may be a symptom of the competition between SRS and FWM described in Section 3.1. Supercontinuum generation is known to amplify the intensity noise of the pump laser [24]. The energy fluctuations of our pump laser was measured to be 1.8%. A pump laser with lower technical noise should improve the output pulse-to-pulse stability, although supercontinuum generation also has some fundamental noise limitations [24]. Even with lower output noise, a calibrated photodiode is clearly necessary to monitor each laser pulse during data acquisition.

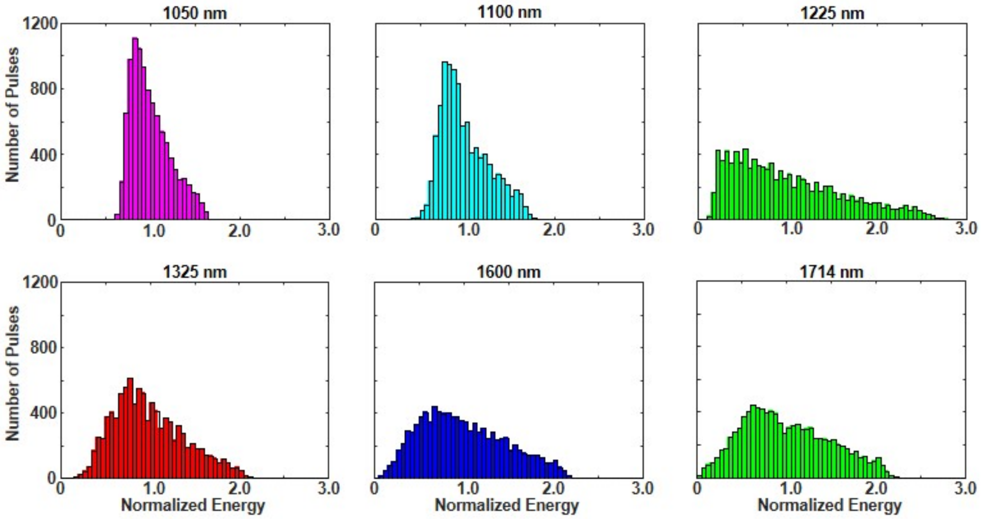

Fig. 7. Histogram of laser pulse energy measured over 10,000 pulses at each output wavelength. The pulse energy is normalized with respect to the mean energy at each wavelength.

As shown in Fig. 6, our supercontinuum source also produces significant energy at visible wavelengths, which is not possible with our previous SRS-based sources. Using 40 nm bandwidth filters, the pulse energy at 850 and 750 nm is measured to be 1.6 and 0.8 μJ, respectively. These shorter wavelengths would be useful for applications involving hemoglobin [27, 28]. Performing OR-PAM at both visible and infrared wavelengths will require careful attention to the color correction of optics. When using achromatic microscope objectives, we observed that the 1600 and 1714 nm pulses have a slightly different focal depth (≈1 mm) compared to the shorter wavelengths. A visible/infrared OR-PAM system would ideally use apochromatic objectives with ultra-broadband color-correction.

5. Conclusions

We have demonstrated multispectral OR-PAM of lipids between 1050 – 1714 nm using a pulsed supercontinuum laser. Lipids are imaged with high contrast at 1714 nm, despite the low pulse energy at this wavelength. Future work includes using a longer photonic crystal fiber to increase pulse energy, compensating pulse-to-pulse fluctuations, and performing OR-PAM at both near-infrared and visible wavelengths. We believe our system's wavelength flexibility makes it promising for a variety of OR-PAM applications such as label-free histology of lipid-rich tissue and imaging small animal models (e.g. zebrafish) of disease.

Funding

The authors gratefully acknowledge funding from the Union College Undergraduate Research Program and previous funding from the National Science Foundtion grant CBET-1157994.

Acknowledgments

The authors thank Prof. Roman Yukilevich and Prof. Quynh Chu-LaGraff for the fixed Drosophila larvae. We are grateful to the reviewers for their helpful suggestions in improving this manuscript.

Disclosures

The authors declare that there are no conflicts of interest related to this article.